Plasma Physics and Controlled Fusion

Commissioning of the tracer-encapsulated solid pellet (TESPEL) injection system for Wendelstein 7-X and first results for OP1.2b

To cite this article: R Bussiahn *et al* 2024 *Plasma Phys. Control. Fusion* **66** 115020

OPEN ACCESS
IOP Publishing
Plasma Physics and Controlled Fusion
Plasma Phys. Control. Fusion **66** (2024) 115020 (15pp)
https://doi.org/10.1088/1361-6587/ad8185

Commissioning of the tracer-encapsulated solid pellet (TESPEL) injection system for Wendelstein 7-X and first results for OP1.2b

R Bussiahn[1,*], N Tamura[2,3], K J McCarthy[4], B Buttenschön[1], C Brandt[1], A Dinklage[1], A Langenberg[1] and the W7-X Team[5]

[1] Max-Planck-Institut für Plasmaphysik, Greifswald, Germany
[2] National Institute for Fusion Science, National Institutes of Natural Sciences, Toki, Japan
[3] The Graduate University for Advanced Studies, SOKENDAI, Toki, Japan
[4] Laboratorio Nacional de Fusión, Centro de Investigaciones Energéticas, Medioambientales y Tecnológicas, Madrid, Spain

E-mail: rene.bussiahn@ipp.mpg.de

Received 18 June 2024, revised 19 September 2024
Accepted for publication 30 September 2024
Published 15 October 2024

Abstract

A new tracer-encapsulated solid pellet (TESPEL) injection system was successfully commissioned for the stellarator fusion experiment Wendelstein 7-X (W7-X) during its OP1.2b operational campaign. TESPELs are polystyrene encapsulated solid pellets loaded with tracer impurities that have been employed in other stellarator devices for impurity transport studies. During the OP1.2b campaign approximately 140 pellet injections were performed with a successful delivery rate of 89%, thus this system has proven to be very reliable. Here, the experimental set-up and methodology are described first. In addition, it is outlined how, through the analysis of TESPEL time-of-flight signals and of the temporal evolution of line emissions originating from shell and tracer species as well as comparisons with ablation models, the radial localization of the deposited tracer is determined. This contribution also provides a general overview of the TESPEL injector performance during OP1.2b, discusses the global effects of TESPEL injections on W7-X plasmas and reports on first results in terms of a summary of TESPEL injections, plasma response to TESPELs, the post-deposition evolution of tracer spectral emission lines and soft x-ray emissions.

Keywords: impurity transport, Wendelstein 7-X, tracer impurity localization

---

[5] See Pedersen *et al* (https://doi.org/10.1088/1741-4326/ac2cf5) for the W7-X Team.

[*] Author to whom any correspondence should be addressed.

1. Introduction

Impurity control is a critical issue on the pathway to steady-state magnetic confinement fusion reactor operation scenarios. It is well known that increasing impurity confinement in high density plasmas can lead to impurity accumulation with subsequent radiation collapse, in particular in helical devices [1]. This is recognized as a potential bottleneck on the pathway to the development of a stellarator based fusion reactor. For instance, impurities, released by high-energy plasma particles impacting on the inner walls of fusion machines, can dilute the plasma and can represent, via ionization and recombination processes, a significant loss channel for plasma heating. Moreover, if the impurity concentration exceeds a certain limit - e.g. due to transport and accumulation in the plasma core—and radiation losses grow, radiation collapse occurs as the supplied heating power can no longer sustain the plasma. Nonetheless, impurity injection-based experiments have allowed effective impurity control to be achieved for some plasma regimes, for instance the HDH-mode in the W7-AS device [2] and the impurity hole phase in the Large Helical Device (LHD) [3]. With the start-up of the optimized stellarator Wendelstein 7-X (W7-X) device [4] and the installation of water-cooled divertors, which will allow long-pulse operation [5], the search for suitable operation scenarios that avoid impurity accumulation has become a critical task.

In order to study impurity transport processes under well controlled experimental conditions, methods such as gas puff, laser blow-off (LBO) and impurity pellet injection have been employed to date for a wide range of magnetic confinement devices [6–8]. Whereas the first two methods deposit tracers close to the plasma edge, which are subsequently transported into and about the plasma, the tracer-encapsulated solid pellet (TESPEL) method has the unique advantage of releasing its tracer(s) directly in the core of the plasma once ablation of the surrounding protective polystyrene shell has exposed them to the hot plasma [9]. Additional advantages include pre-selection, to a certain extent, of the tracer deposition depth, selection of the quantity of tracer material enclosed with the pellet and a large number of elements that can be injected compared to LBO or gas puff. The deposition depth is determined mainly by the plasma electron temperature and density profiles, and to a certain extent by the shell geometry (diameter, wall thickness) and the TESPEL speed. These are important advantages for impurity transport studies which have highlighted, for instance in LHD, the importance of location (inside/outside a last-closed flux surface) of the impurity source on impurity behaviour in the plasma [10].

A primary aim of the W7-X project is to achieve long-pulse discharges; thus, it is necessary to develop successful operation scenarios that avoid impurity accumulation in this device. Given the successful installation and operation of TESPEL systems on other stellarator devices [11, 12], it was considered that a dedicated system could provide valuable information for resolving the impurity challenge in W7-X and allow inter-machine comparisons. Hence, a dedicated TESPEL system was installed and integrated on W7-X [13, 14].

Here, the commissioning and some first results of this system are described and discussed. This system design and operational principals are similar to those of the TESPEL system installed on LHD and due to comparable machine geometries, the shell types employed previously on LHD are also used here. This paper provides a general overview of the TESPEL injector performance during its first experimental campaign OP1.2b. The main purpose of this paper is to present the applied method for the precise localisation of the tracer deposition area, as its knowledge is an important prerequisite for further impurity transport studies (which are outside the intention of this paper). Furthermore, the global effects of TESPEL injections on Wendelstein 7-X plasmas are discussed and first measurements of the x-ray emissivity in the poloidal cross-section of the plasma are presented, which provide information about the temporal evolution of the spatial distribution of the impurity tracers after a TESPEL injection. We discuss the effects and methods in this paper on the example of a single, representative Wendelstein 7-X experiment, which was performed in standard magnetic field configuration with electron cyclotron resonant heating (ECRH) only. The effects discussed are typical for this type of discharges and have been partly discussed in other papers investigating TESPEL injections (see [15, 16]).

2. Experimental setup and methodology

2.1. The stellarator Wendelstein 7-X

The Wendelstein 7-X (W7-X) device, with major machine radius of 5.5 m, is a large stellarator that confines a toroidal plasma with an effective minor plasma radius of about 0.5 m. Its first experimental operation campaign, OP1.1, was undertaken in 2015 and 2016 [4]. Seventy superconducting coils produce a steady-state magnetic field with a flux density up to 3 T at the magnetic axis and the modular arrangement of these coils allows high-flexibility when creating its magnetic configurations. During the OP1.2b experimental phase [17], when the TESPEL system was commissioned, up to 8 MW of ECRH, with resonant frequency of 140 GHz for second harmonic heating, was available. Moreover, rotatable launch mirrors permit the radial localization of the ECRH heating power (on- or off-axis) in the plasma. Two neutral beam injection (NBI) heating systems with a nominal 4 MW of heating power and 55 kV beam energy (full energy component) were also available for OP1.2b. The total pulse length of the NBIs was limited to 5 s whereas the ECRH's were steady-state systems. The NBIs can also be used for active plasma diagnostic purposes. For this they are operated in pulsed mode. After the installation of water-cooled divertors, the W7-X device will be dedicated to long-pulse operation, i.e. up to 30 min [18]. However, during the OP1.2 campaign, when passively cooled

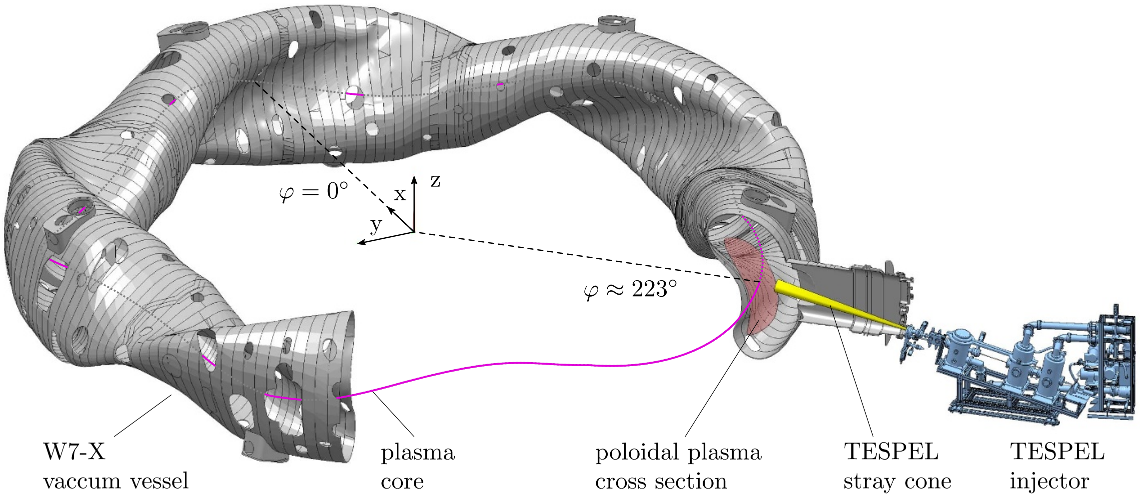

Figure 1. Schematic representation of the W7-X vacuum vessel and the TESPEL injector assembly showing the poloidal plasma cross section of the injection plane and its toroidal angle φ.

divertors were used, the pulse length was limited to less than 10 s. Finally, the plasma working gas is hydrogen or helium for the TESPEL injections summarized in this paper and the central electron temperature, $T_e(0)$, ranges from 1 keV to 8 keV when TESPEL injection occurs.

2.2. The TESPEL injector on W7-X

The TESPEL injector on W7-X (cf figure 1 and further details in [13]) is a blower-gun type system that basically consists of a rotatable pellet storage disk from which a TESPEL is shot through a barrel (inner diameter = 1 mm) into guiding tubes directing it to the main W7-X vacuum chamber. TESPELs are accelerated by means of a fast valve ($t_{\mathrm{open}} \approx$ 2 ms) where helium is used as propellant gas, typically at a pressure of 30–40 bar. Multiple gaps between the individual guiding tubes make it possible to effectively remove the propellant gas into three expansion chambers. The effectiveness of this differential pumping system was demonstrated in a trial run in which a gas shock without a TESPEL (blank shot) was triggered. When monitoring the W7-X pressure sensors, no pressure increase could be measured inside the vacuum vessel. After each TESPEL injection, the vacuum pumps of the TESPEL injection system typically require about 3 min to reduce the pressure to its pre-injection value. In the first expansion chamber, which adjoins the TESPEL disk, a base pressure of 5×10^{-4} mbar was obtained, while in the other two expansion chambers pressures of $p < 2 \times 10^{-8}$ mbar were reached.

The mechanical integration of the TESPEL system to W7-X was reported in [14]. After its attachment to the stellarator, the position of the injector within the torus hall was determined by laser-tracking (typical accuracy 0.3–0.6 mm) [19]. From these measurements, the coordinates of the injection axis and its intersection with the light barriers in the time-of-flight module were calculated.

The injector control system, operable from the W7-X control room via a software panel, is based on SIEMENS S7-300 PLC-components and is connected to a local safety system which itself communicates with the W7-X central safety system. In cases of emergency, all vacuum pumps of the injection system are switched off, several gate valves are shut, safety valves in the helium gas supply line are closed and the power supplies of the two lasers for time-of-flight measurements as well as of the fast valve controller are switched off. These power supplies are also controlled by a release signal which is set by the central safety system. In order to prevent a TESPEL injection into the W7-X vacuum vessel when plasma is not present, which might cause damage to the inner wall carbon tiles, an additional optical interlock was foreseen to detect and confirm visible plasma radiation immediately before an injection event. In case of insufficient signal intensity, the triggering of a TESPEL injection should be interrupted. However, in tests, the signal intensity output from the photo-diode was too low to be processed successfully by the discriminator circuit and hence to interrupt the triggering. This important safety mechanism has been reviewed.

2.3. TESPEL capsule geometry

A TESPEL consists of a spherical polystyrene $(C_8H_8)_n$ capsule, which contains a pre-selected amount of impurity tracer(s). In order to ensure comparability for impurity transport studies made using TESPELs in LHD and W7-X which have similar machine geometries, the same shell types and sizes are used for experiments in both devices (see table 1). This is done because varying the outer capsule diameter and wall thickness allows control of the shell ablation duration and therefore some control of the penetration depth. These parameters determine also the amounts of hydrogen and carbon being released to the plasma. Moreover, their quantities, together with the amount of tracer impurities, determine the

Table 1. Polystyrene capsule types used for W7-X experiments. Here, D_{out} is the capsule's outer diameter, D_{in} is the diameter of the empty core, and D_{wall} is the wall thickness.

TESPEL name	Capsule type	D_{out} (μm)	D_{in} (μm)	D_{wall} (μm)
B900	Ball	900	300	300
B700	Ball	700	250	225
S700	Shell	700	550	75

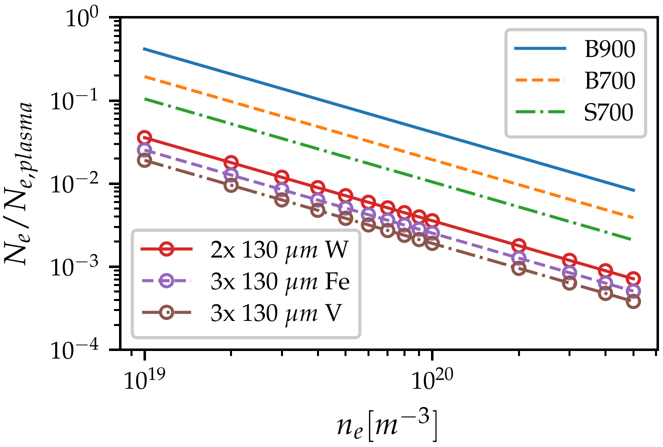

Figure 2. Ratio between the number of TESPEL-derived electrons and the background plasma electron population for representative electron densities in W7-X experiments. Shown are the contributions of three shell types used in OP1.2b (upper right legend, for details see table 1) and three typical tracer loads (lower left legend, labels indicating the number of powder grains a TESPEL is filled with, the grain diameter and the material).

level of background plasma perturbation. Figure 2 illustrates the ratio between the number of TESPEL-derived electrons and the background plasma electron population for representative electron densities in W7-X experiments for the three shell types used during OP1.2b and for typical tracer loads. It is seen therein that typical tracer amounts cause a small increase in the overall electron number, this being less than 5%. The shell-related data in the diagram point to the importance of suitable shell geometry selections. It is seen that the ablated hydrogen and carbon atoms can significantly contribute to the overall electron inventory in the plasma, especially for background plasma electron density conditions in the region close to a few times $1 \times 10^{19}\,\mathrm{m}^{-3}$. Thus, the TESPEL type best suited for such conditions is the 700 μm diameter shell-type whereas the use of 900 μm ball-type is best limited to experiments undertaken when the electron density is close to, or above, $1 \times 10^{20}\,\mathrm{m}^{-3}$.

2.4. TESPEL ablation light detection

The basic technical features of the TESPEL observation system are described in [13]. Data acquisition of the optical signals from the 8-channel filterscope and the spectrometer is performed by means of an analogue-to-digital converter (ADC) at a rate of $2\,\mathrm{MS\,s}^{-1}$. It's synchronization to the W7-X central timing system [20] was controlled via MDSplus [21]. Three RedPitaya STEMlab 125–14 units, also integrated into the MDSplus system, acted as digital delay generators to trigger the ADC and to control the TESPEL injection time as well as two gate valves along the injection path.

Next, using an ultrafast-frame imaging camera (Photron Fastcam SA5, up to 600 kHz), the spatio-temporal evolution and drift of the ablation cloud can be followed by selective imaging of emission lines of hydrogen and carbon. It has been shown that TESPELs, injected into W7-X, follow straight trajectories within the plasma without being deflected, unlike cryogenic pellets [16]. Therefore, locating the deposited tracers in the plasma can be based on a simple time-of-flight measurement. From the comparison of the shell and tracer ablation signals and the correlation with the TESPEL velocity (determined by the time difference between the signals of the two light barriers of the time-of-flight module), the exposure and deposition of the tracer to plasma after ablation of the protective polystyrene envelope can be calculated.

2.5. Shell and tracer ablation analysis

As soon as a pellet enters the hot plasma, ablated particles detach from the outer shell surface and initially form a neutral cloud around the travelling pellet. This cloud, which shields the shell from direct plasma electron impacts, detaches occasionally from the TESPEL and as neutrals become ionized, the electrons and ions start to gyrate along the magnetic field lines leading to an expansion of the ionized cloud as observed by the ultrafast-frame imaging camera [16]. In the case of cryogenic pellets, detached clouds are observed to be accelerated outwards with the result that the pellet particle deposition profile is displaced radially outwards when compared to the ablation light profile [22]. Such outward displacement arises from interactions between the background magnetic field and an internal electric field that develops across the partially ionized cloud (plasmoid) due to charge separation. This drifting continues until expansion of the cloud in the radial and toroidal directions finally leads to equalization of the cloud density with the background plasma. It is known that the temporal evolution of the drift velocity is inversely proportional to ion mass [23], thus the $\vec{E} \times \vec{B}$ outward drift will be significantly reduced for heavier ions when compared to that of hydrogen. Indeed, this was experimentally confirmed for TESPEL and hydrogen pellets in the stellarator TJ-II in which significant differences were observed between H-pellet and TESPEL particle deposition profiles [24]. It can therefore be assumed that, once the tracer is exposed to the plasma after the ablation of the shell, the tracer ions experience little or no outward drift and the radial position at which the light from the tracer impurity is observed represents the location of the tracer deposition. Subsequently tracer ions will undergo ionization and recombination as well as inward and outward transport. These latter processes can be followed by a range of diagnostic systems on W7-X. Figure 3 shows the location of the more important diagnostics for impurity transport studies as well as cross-sections of magnetic flux surfaces (based on calculations using the code VMEC [25, 26]) and the intersection points of field lines, starting along the TESPEL injection trajectory in the direction of

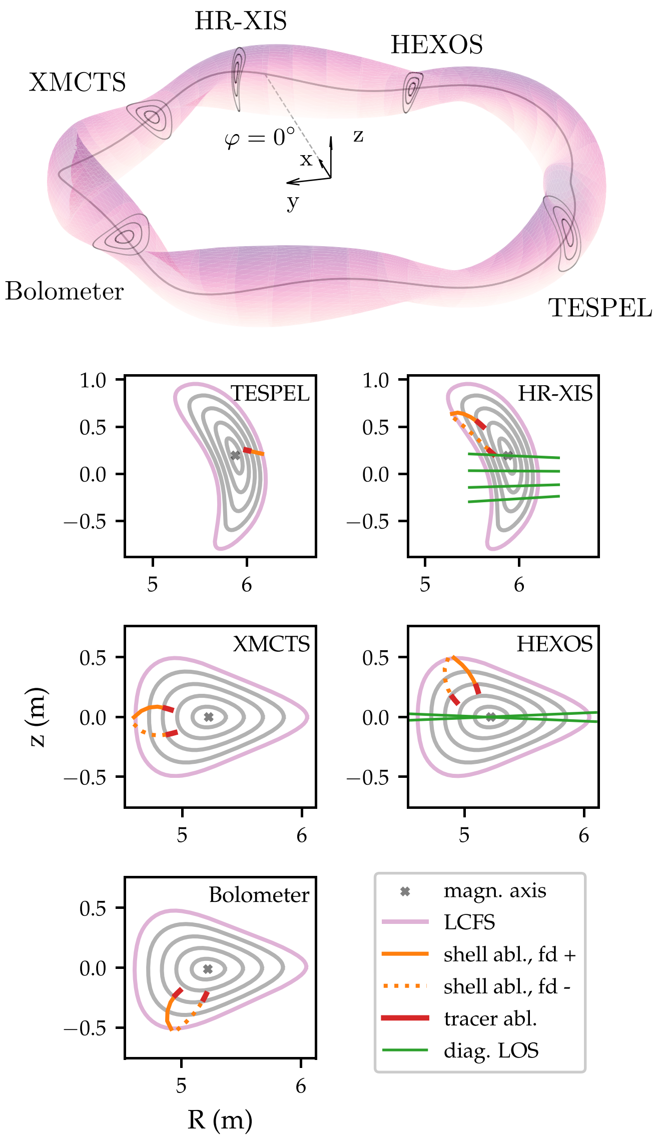

Figure 3. Sketch of the confined plasma (top), showing the locations of the main impurity transport diagnostics available for TESPEL and (bottom) poloidal plasma cross-sections at the same positions. Cross-sections show the locations of the magnetic axis, the last closed flux surface (LCFS) and inner flux surfaces. Additionally, characteristic lines-of-sight (LOS) are depicted for the HEXOS and HR-XIS diagnostics. Solid and dotted lines in orange illustrate the initial intersection points of field lines in positive (fd+) and negative (fd−) magnetic field directions for particles released during the ablation processes of the outer TESPEL capsule along the TESPEL injection trajectory. Red areas at the end of the orange lines indicate intersection points with field lines in the spatial region of initial tracer release.

positive and negative field direction, in the related diagnostics planes.

2.6. *Tracer deposition localization*

Ablation light is collected through an optical viewport mounted on the same vacuum vessel port as the TESPEL injector (the viewport to plasma edge distance is ≈2.35 m). Outside the viewport, a beam splitter divides the light so part of the light passes through it to a collimating lens that focuses it onto an optical fibre for transfer from the W7-X experimental hall to a laboratory located ≈40 m away. The light reflected by the beam splitter is directed onto a lens that, in turn, focusses it onto a fibre optic light guide for transfer to the fast-frame imaging camera. In the laboratory, the transmitted light is divided again using a fibre optic fan-out. Part of this light is directed to a high-resolution spectrometer while the remaining light is transferred to the filterscope system. This latter system is equipped with narrowband transmission filters and photomultiplier tubes. The central wavelengths of these filters were chosen to be close to the wavelengths of the predicted intense spectral lines emitted by the atomic states of carbon, hydrogen and the tracers of interest.

The practical evaluation of the ablation signals revealed that the optical filters in the filter scope had been selected with too broad a bandwidth, particularly for the C I and the tracer channels. While the H_α-filter had a narrow bandwidth of 1 nm, all other filters had a full width at half maximum (FWHM) of 10 nm (see the filter list and details in table III of reference [13]). As a result, unwanted line radiation and broadband recombination continuum radiation/bremsstrahlung [27] contributed significantly to the signal level in almost all channels and a clear separation between the contributions of shell and tracer ablation radiation required some effort. To address this problem, we used the following procedures (cf figure 4):

1. Scaling of shell and tracer signals (figure 4(a))
   (a) Background level (BGR) determination and subtraction for shell and tracer signals
   (b) Normalization of the H_α-signal to its maximum intensity $H_\alpha^{\max}$
   (c) Determination of the shell ablation start: where H_α-signal level exceeds BGR $+ 2 \times$ the standard deviation of BGR
   (d) Scaling of the tracer signal by fitting a constant factor to match H_α- and tracer signal levels in the range between the shell ablation start and $0.8 \times H_\alpha^{\max}$
2. Calculation of a differential signal (figure 4(b): tracer - H_α)
3. Calculation of a relative signal (figure 4(c): tracer/H_α)
4. Determination of the transition between shell and tracer ablation and of the tracer ablation end (dashed grey bars in figure 4) by comparing the scaled/normalized ablation signals with the differential and the relative signals. It turned out that the differential signal alone was not sufficient to clearly indicate this transition. Instead, the most robust information was derived from the tracer / H_α signal where the zero point right before the pronounced increase in the relative intensity was taken. As small oscillations in the relative signal made it difficult to determine this specific zero point automatically, features in the differential signal and in the normalized/scaled signals helped making the final decision visually.

The radial localisation of the tracer deposition in the plasma was determined from the detected light emissions of the shell or tracer species and the TESPEL velocity. In a first

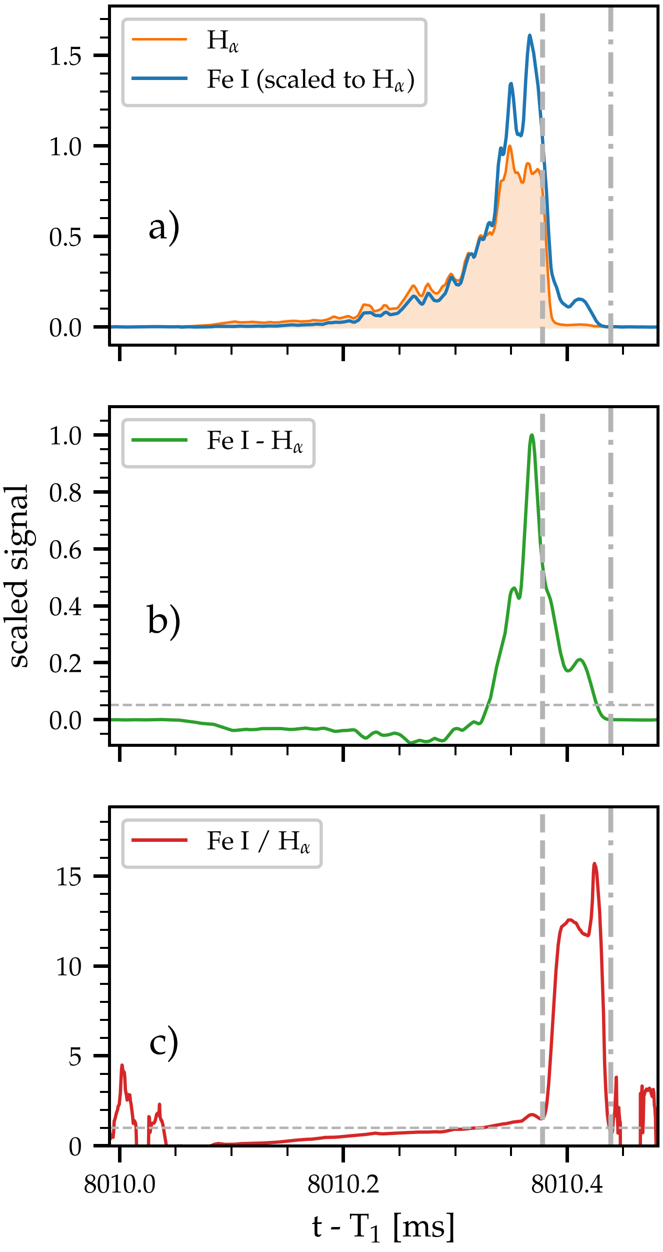

Figure 4. Comparisons between signals from the Fe I—tracer filterscope and the H_α shell filterscope channels for W7-X experiment #20180906.38. (a) Fe I signal scaled to the H_α signal. The Fe I scaling factor is calculated in a non-linear square fit in the range between shell ablation start and the time when the H_α signal reaches 80% of its maximum value. (b) Scaled Fe I signal minus H_α signal and (c) ratio of the scaled Fe I signal to the H_α signal. The vertical lines refer to the range which was identified as the actual contribution of the ablating tracer particles to the Fe I signal. T1 is the start time of plasma heating.

approach, the TESPELs were assumed to move along the nominal injection axis. However, initial calculations produced unexpected results, in particular the calculated location for the onset of shell ablation was too deep within the confined plasma. However, such behaviour had not been observed in the TESPEL experiments at LHD or TJ-II. Instead, ablation of TESPELs typically starts when passing the last closed flux surface (LCFS). As a systematic source of error (about 3%–4%), an inadequately accurate measured distance between the two light barriers of the ToF-module was identified. Furthermore, it turned out that even small angular deviations from the nominal injection axis in combination with the given curvature of the LCFS can have a significant effect on the result. To tackle this, ≈400 vectors were defined within a scattering cone with an opening angle of 2.2° (cf figure 5), leading to a spatial resolution of $\delta s \approx 5\,\mathrm{mm}$ in the tracer deposition zone. The coordinates of the LCFS were derived from VMEC-calculations [25, 26] that were supplied as a list of magnetic reference configurations for all experiments of the W7-X OP1.2b campaign. Finally, the most probable injection vector was determined by finding the one for which the distance between the start of the shell ablation and the LCFS was minimal.

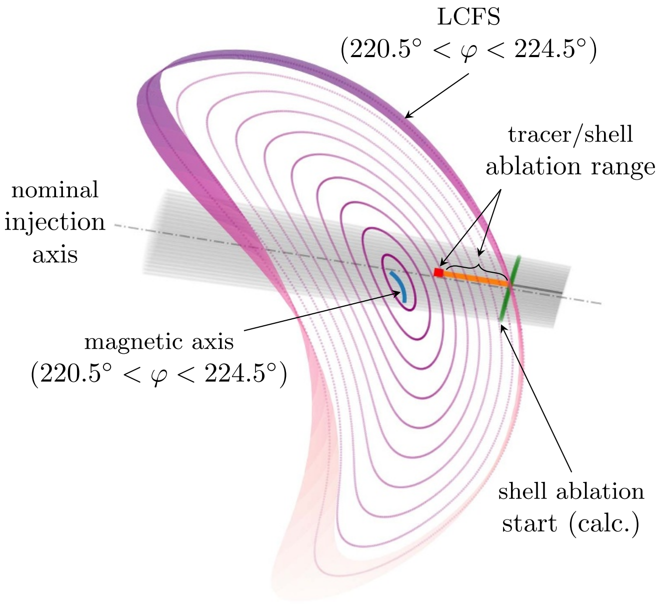

Figure 5. 3D-sketch of the plasma poloidal cross-section in the TESPEL injection plane, showing part of the magnetic axis (light blue) and of surrounding flux surfaces. TESPELs are injected from the low-field side (right side in this picture). The nominal injection axis is indicated by the dash-dot grey line. The estimated positions (from time-of-flight analysis) of the start of shell ablation for all considered trajectories within the scattering cone (light grey region surrounding the nominal injection axis) form a spherical cap (green). The most likely trajectory (solid grey line) is determined by calculating the intersection of the shell ablation start positions with the last-closed flux surface (LCFS). Regions of shell and tracer ablation along the most likely trajectory are depicted by orange and red lines, respectively.

The transport behaviour of the impurities after deposition depends strongly on the specific shape of the kinetic electron profiles and the associated gradients. For detailed transport studies, it is therefore essential to know the radial position at which the tracer impurities were originally deposited. The method of deriving the penetration depth from time-of-flight measurements depends on certain quantities that are not measured directly, e.g. the location of the LCFS or the specific

Table 2. Neutral gas shielding scaling law coefficients used for TESPEL ablation simulations. Here with the shielding factor $\eta = 0.4$, the sublimation energy of a C_8H_8-molecule $\varepsilon = 1.0\,\text{eV}$, the electron mass m_e, the atomic mass $A_p = 6.5\,\text{u}$ and the atomic mass unit u. $Z_p = 3.5$ and $\varepsilon_\text{CH} = 0.0625\,\text{eV}$ are the nuclear charge number and the sublimation energy of an 'average C_8H_8 atom' and $\gamma = 8/6$ is the gas adiabatic index.

i	Reference	c_i	α_i	β_i	δ_i
1	[28]	$\frac{2\eta}{\varepsilon}\sqrt{\frac{2\pi}{m_\text{e}}}$	1	3/2	2
2	[29], (equation 15)	$4 \times 10^{15} \cdot A_p^{-1/3} \cdot Z_p^{-2/3}$	1/3	11/6	4/3
3	[29], (equation 20)	$1.94 \times 10^{14} \cdot \varepsilon_\text{CH}^{-0.16} \cdot A_p^{-0.28} \cdot Z_p^{-0.56} \cdot (\gamma - 1)^{0.28}$	0.45	1.72	1.44

TESPEL trajectory. In order to validate the method for calculating the most likely injection trajectory, and thus determine the radial position of the initial tracer deposition, the shell ablation signal is compared with results obtained from different ablation rate scaling laws based on neutral gas shielding models proposed by Khlopenkov *et al* [28] and Sergeev *et al* [29]. The equations can be expressed in a generalized form, where $\text{d}N_i/\text{d}t$ denotes the ablation rate, n_e [cm^{-3}] and T_e [eV] represent electron density and temperature, respectively, and r_p [cm] is the pellet radius. The related coefficients are given in table 2:

$$\frac{\text{d}N_i}{\text{d}t} = c_i \cdot n_\text{e}^{\alpha_i} \cdot T_\text{e}^{\beta_i} \cdot r_p^{\delta_i}. \quad (1)$$

Good agreement between the end of the experimentally observed shell ablation phase and that predicted by the neutral gas shielding scaling laws can then be seen as a proof for a properly calculated injection trajectory. It should be noted, that all the afore mentioned scaling laws predict the ablation rate for a single atom of a specific material. In case of more complex materials such as C_8H_8, the ablation rate for the molecule $\dot{N}_m$ is just the rate $\dot{N}_{\hat{a}}$ for an 'average' atom, divided by the number of atoms that are contained in a single molecule n_{apm}. Thus

$$\dot{N}_m = \frac{\dot{N}_{\hat{a}}}{n_{apm}}. \quad (2)$$

2.7. Tracer spectral line emission

W7-X is equipped with a large number of different spectroscopic diagnostics covering a broad wavelength range from x-ray to the near-infrared [30]. In order to track the post-deposition temporal evolution of the line emission of the injected tracers, two spectrally resolving diagnostics, the high efficiency XUV overview spectrometer (HEXOS) and the high resolution x-ray imaging spectrometer (HR-XIS) are prominent [31, 32]. Thus, focussing on iron as the tracer impurity for this work, the principal accessible emission lines for HEXOS, in the wavelength range 5–35 nm, are shown in table 3 for several ionization states. Several of these will be used later to provide an example of the temporal evolution of the impurity line emissions and to derive the radiation decay time from semi-logarithmic signal plots. Such a radiation decay time can then be considered as a proxy/measure for the impurity confinement time.

Table 3. Characteristic Fe spectral emission lines detected by the HEXOS system for TESPEL injections [33]. The wavelengths, as well as upper and lower transition levels, are shown. The *'s indicate spectral lines used in figure 14. (1) The Fe XXV spectral emission at ≈0.185 nm (He-like state) is measured by the HR-XIS diagnostic [32].

Spectroscopic notation	Wavelength [nm]	Lower level	Upper level
Fe VIII	9.837	$3p^6\ 3d$	$3p^6\ 6f$
Fe XIV	21.133	$3\ s^2\ 3p$	$3\ s^2\ 3d$
Fe XV*	28.416	$2p^6\ 3\ s^2$	$2p^6\ 3\ s\ 3p$
Fe XVI	33.541	$2p^6\ 3\ s$	$2p^6\ 3p$
Fe XVIII	10.394	$2\ s^2\ 2p^5$	$2\ s\ 2p^6$
Fe XX*	11.870	$2\ s^2\ 2p^3$	$2\ s\ 2p^4$
Fe XXI	14.573	$2\ s^2\ 2p^2$	$2\ s\ 2p^3$
Fe XXII	13.581	$2\ s^2\ 2p$	$2\ s\ 2p^2$
Fe XXIV*	19.203	$1\ s^2\ 2\ s$	$1\ s^2\ 2p$
Fe XXV$^{\star,(1)}$	≈0.185	$1\ s^2$	$1\ s\ 2p$

2.8. Radial and poloidal impurity distribution measured by soft x-ray emission

The soft x-ray multi-camera tomography system (XMCTS) of Wendelstein 7-X [34] measures the x-ray emissivity in the energy interval 1–12 keV in the triangular poloidal cross section along 360 sight-lines using 20 slit cameras (cf figure 11). The two-dimensional emissivity patterns are obtained by tomographic inversion (here the regularization based on the minimum Fisher information [35] is applied). Its time resolution is 0.5 μs and the average spatial resolution is approximately 4 cm.

Line radiation and continuum radiation add up to the total x-ray emissivity. X-ray line radiation is proportional to $n_\text{e} n_Z$ where n_e is the electron density and n_Z the ion density. For continuum radiation, consisting of contributions from bremsstrahlung and recombination radiation, the emitted power is proportional to $\Sigma_i\, n_\text{e} n_i\, Z_i^2\, T_\text{e}^{1/2}$ [36]. For both, line and continuum radiation, a direct proportionality to electron and ion density is given. During the ablation of a TESPEL and subsequent transport processes, the densities are locally increased. The effect of tracer impurities on the x-ray emission is particularly enhanced by the Z^2 dependence of the continuum emission. Taking into account that the effect of $T_\text{e}^{1/2}$ on continuum radiation is less pronounced compared

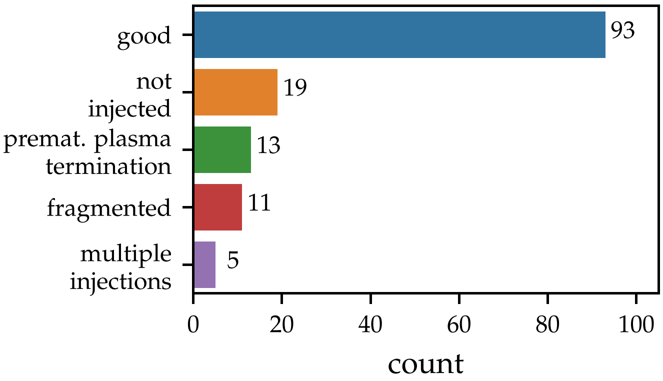

Figure 6. Summary of TESPEL injections during OP1.2b. Here, 'good' is an intact TESPEL entering the LCFS, 'not injected' is a TESPEL lost before entering W7-X, 'premat. plasma termination' is plasma termination or collapse prior to injection, 'fragmented' is a broken TESPEL entering the LCFS and 'multiple injections' is more than one TESPEL during an experiment.

to the other parameters, the analysis of the x-ray emissivity can be considered for interpreting the poloidal and radial distribution of the injected tracer impurities, although the diagnostic method cannot separate between the three different contributions to the total x-ray emissivity.

3. Results

3.1. Global injection summary

During W7-X's 1.2b operational phase, 141 experiments involving TESPEL injections were performed. In total, 93 TESPELs were successfully injected into the W7-X plasma (see figure 6). Due to a malfunction in the TESPEL disc or due to trigger errors, 19 TESPEL were not accelerated on not injected. Events such as plasma non-ignition or premature termination could not be detected automatically due to problems with the optical interlock. In some cases, the injection of a TESPEL into the main vacuum vessel could be interrupted manually, but in a few other cases this was not possible and the unablated TESPEL then most probably hit the inner wall of the vacuum vessel. However, video inspection after campaign completion did not reveal any damage to the mounted carbon tiles. In addition, 11 TESPELs entered the plasma partially fragmented. It is likely that they have suffered strong impacts on the inner tubing walls during their transfer through the guiding tube system. Finally, in 5 cases, multiple pellets were injected unintentionally. This occurred accidentally and may have been be to human error during the disk loading procedure or to storage chamber skipping during in operation. Nonetheless, even such a severe plasma perturbation did not lead to radiation collapse. Indeed, both of the latter events, fragmented TESPELs and multi-injections are easily detected in the signals from the two laser gates of the time-of-flight module. Now, considering the data for 'good' and 'fragmented' injections has allowed an evaluation of the guiding tube system alignment to be made. This analysis results in a transfer probability of 89%. Taking into account 'not injected' and 'multiple injections' cases the overall success of the injection system is 73%.

3.2. Plasma response to TESPEL

The ablation of an injected TESPEL results in the release of a large number of cold electrons and ions which cause a short-lived global perturbation of the plasma (see figure 7). This manifests itself as an instant but small rise (≈5%) in line-averaged electron density and a concurrent but transient drop in electron temperature, seen in the data derived from electron cyclotron emission ($T_{\mathrm{e,ECE_{core}}}$). About 200 ms after injection, T_e recovers to values being even slightly above the temperature before injection. The ion temperature in the core region changes less quickly and less pronounced but slowly rises and finally exceeds the pre-injection value. Spatially resolved measurements (from x-ray imaging crystal spectrometer (XICS) and electron cyclotron emission (ECE), not shown here) exhibit an inwards propagating temperature drop starting at the edge with the injection of a TESPEL, often referred to as cold wave.

The increase in ion temperature after injection may seem counter-intuitive at first glance, but a similar behaviour was observed after injecting a series of cryogenic pellets into W7-X [37, 38] and at the same time an improved energy confinement was noted. The behaviour is explained by the changes in the density profile induced by the ablating pellets and the resulting stronger density gradients, which suppress the ion temperature gradient turbulence, which finally leads to an improved confinement. In [38] it is pointed out that comparable effects with regard to improved energy confinement can also be observed immediately after TESPEL injections.

The diamagnetic energy, W_{dia}, drops for a short term after the injection and then increases slightly and remains so until the electron density and temperature have almost returned to their pre-injection values. Such behaviour is usually accompanied by a decrease in density fluctuations and also points to a suppression of turbulence during this period [39].

Finally, as seen in the bolometer and bremsstrahlung time traces, the global radiation rises instantly and decays again to pre-injection values within a few hundred milliseconds.

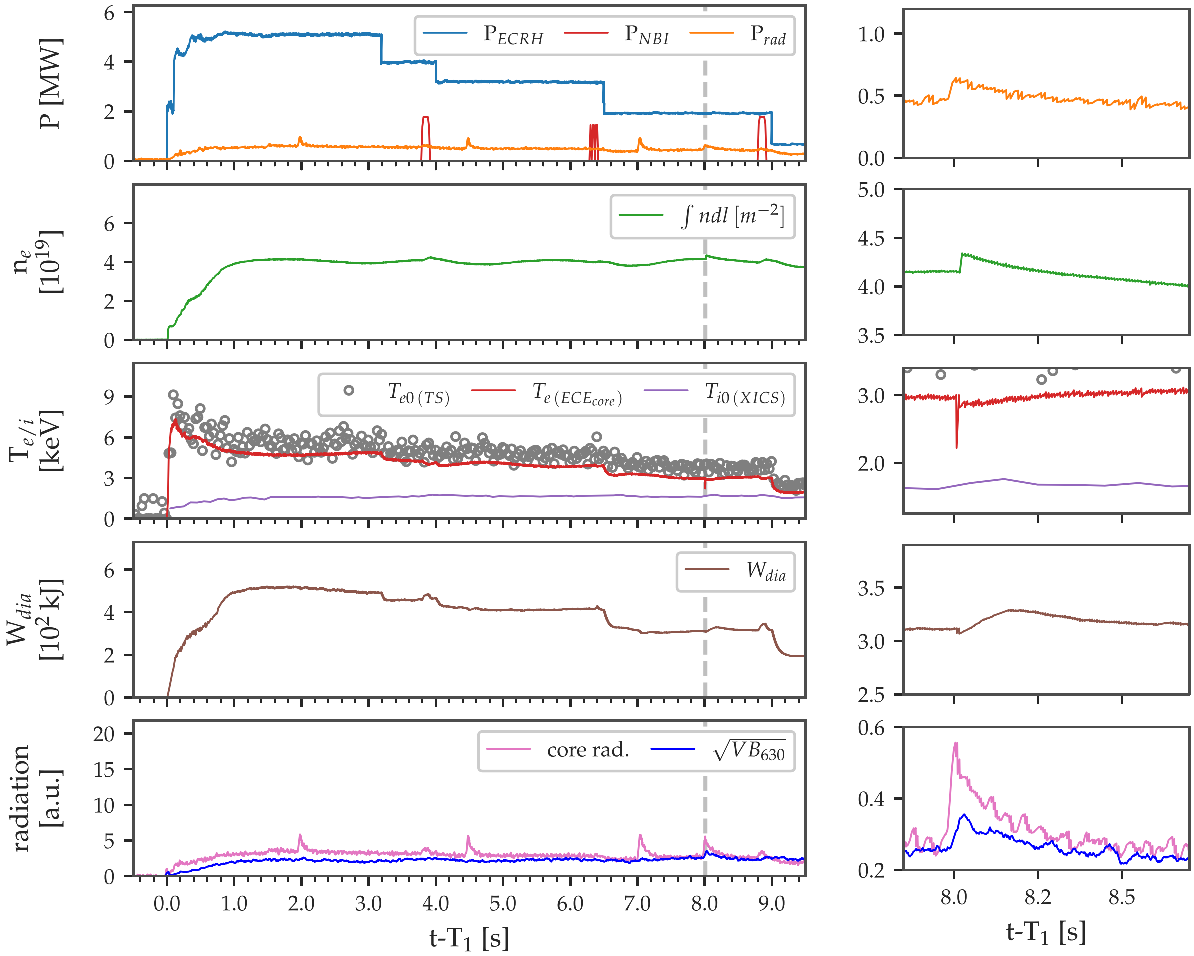

Figure 7. Example of the effects of a TESPEL injection on global plasma parameters (W7-X experiment #20180906.38). The curves show the evolution of electron cyclotron resonance heating power (P_{ECRH}), neutral beam power (P_{NBI}), total radiated power (P_{rad}), line-integrated electron density ($\int ndl$), electron and ion temperatures measured by Thomson scattering ($T_{\mathrm{e,\,TS}}$), electron cyclotron emission ($T_{\mathrm{e,\,ECE}}$) and x-ray imaging crystal spectrometry ($T_{i,\mathrm{XICS}}$), respectively, plasma diamagnetic energy (W_{dia}), and bolometer core channel emission (core rad.) and line-integrated bremsstrahlung emission about 630 nm ($\sqrt{VB_{630}}$). The vertical dash-dash line represents the TESPEL injection time. The diagrams in the right-hand column show part of the same data as on the left side, expanded by a factor of five.

3.3. Shell ablation and tracer deposition

A correct localization of the tracer deposition volume is a very important precondition for impurity transport studies. As pointed out in section 2.6, the actual trajectory within the injection stray cone has a significant influence on the spatial area, where the tracer is initially released. Figure 8 shows the spatio-temporal mapping of selected trajectories and illustrates how the deposition area (calculated from the experimentally observed ablation signals) varies with such trajectories. As seen from equation (1) and the coefficients in table 2, the ablation rate of an injected pellet is strongly influenced by electron temperature, and to a lesser degree by electron density. As an example, predicted penetration depths, obtained using the three sets of scaling law coefficients in table 2, are compared with the experimental ablation profile for W7-X experiment #20180906.38. For this, the kinetic profiles and the confidence levels used as input for predictions are taken from Thomson Scattering measurements (see figure 9). In the same figure, the time reference for the H$_\alpha$ signal is converted to radial positions along plasma normalized radius. Thus, from this figure, an experimental penetration depth of $\rho \approx 0.47$ is determined for the experiment. Next, in the same figure, and considering a 700 μm shell type TESPEL with 80 μm wall thickness, predicted ablation profiles are shown for the three sets of coefficients of table 2. Moreover, the shaded area in figure 9(c) indicates the predicted minimum and maximum end positions for the shell ablation for the most likely trajectory path. This area is obtained using the kinetic profile confidence intervals for all three models.

As noted previously, 93 TESPELs were successfully injected into W7-X plasmas during the 1.2b operational phase. In order to highlight the good reproducibility of tracer deposition, and to demonstrate the possibility to preselect the tracer deposition depth to some degree, TESPEL penetration depths versus central electron temperature are plotted for ‘shell’ and ‘ball’ capsule types in figure 10. Central electron temperature, rather than central electron density, is considered here as the ablation rate is more sensitive to electron temperature than to other variables, i.e. plasma density, TESPEL velocity or

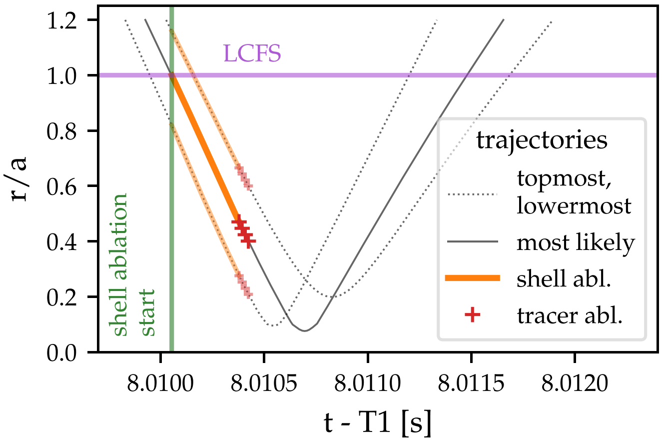

Figure 8. Spatio-temporal mapping of different possible TESPEL injection trajectories for W7-X experiment #20180906.38. Trajectories, labelled as topmost and lowermost refer to trajectories at the upper and lower edge of the scattering cone in figure 5 and result in the shallowest and deepest TESPEL penetrations whereas the 'most likely' trajectory is the one where the shell ablation (orange) starts closest to the last closed flux surface (LCFS). Here $r/a = 1$ is the LCFS and $r/a = 0$ is the magnetic axis. T1 is the start time of plasma heating.

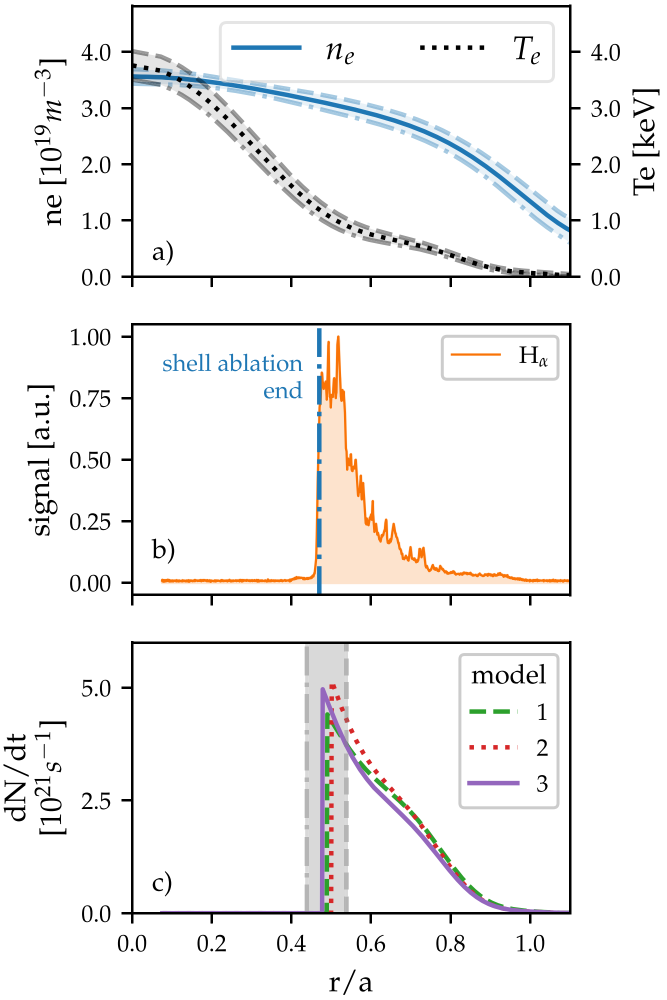

Figure 9. (a) TS electron density and temperature profiles with confidence levels used here to predict shell ablation along the most likely trajectory for W7-X experiment #20180906.38, (b) measured ablation signal (H$_\alpha$ channel) superimposed on the normalized plasma minor radius and (c) results for different neutral gas shielding scaling laws (1: from [28], 2: equation (15) of [29], 3: equation (20) of [29]), taking the TS kinetic profiles of (a) as input. Here, r/a is the normalized plasma radius. The shaded area indicates the predicted minimum and maximum end positions for shell ablation along the most likely trajectory according to the confidence intervals in (a) for all three models.

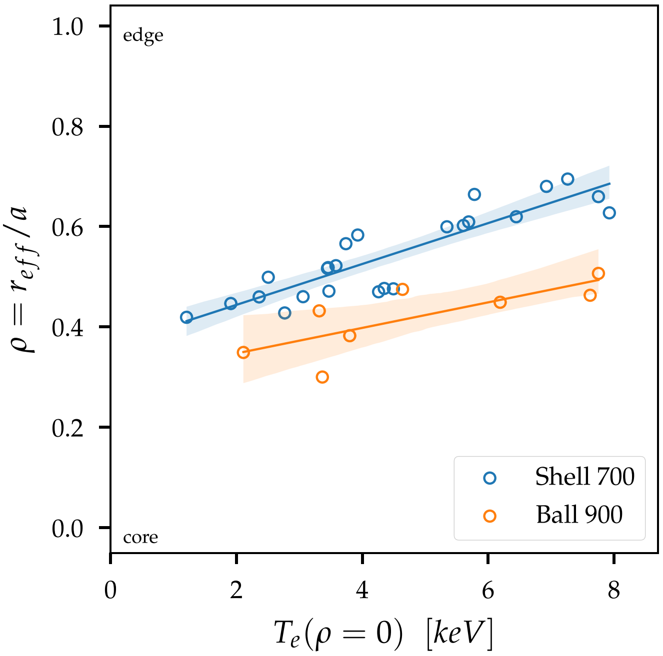

Figure 10. Penetration depth of two different TESPEL capsule types as function of the electron temperature at the plasma core, T_e. Data points refer to the position where the shell ablation ends and the tracer ablation starts, as calculated from filterscope signals. The linear regression lines are added to guide the eye.

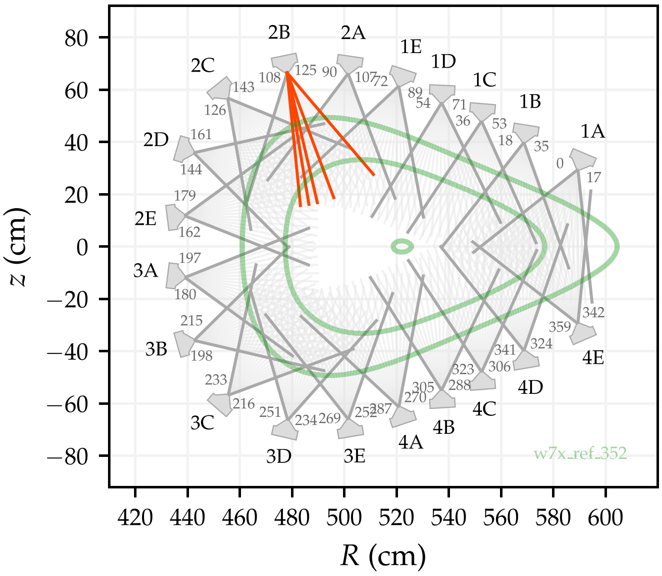

Figure 11. Arrangement of the 20 XMCTS camera heads (1A - 4E), providing 18 lines-of-sight each (grey labels next to the cameras, numbered 0–359). For camera 2B, five selected lines-of-sight are plotted in red, indicating those for which the related time-traces are shown in figure 12. Green curves indicate flux surfaces at the radial positions $r/a = 0.1$, 0.71 and 1.0.

TESPEL radius. This plot shows good radial tracer deposition reproducibility and thus confirms the possibility to preselect a radially shallower or deeper tracer deposition by choosing the capsule type.

3.4. Post-deposition impurity transport and tracer evolution

The scientific goal of the TESPEL method is to deposit a quantified source of known impurities, either intrinsic or non-intrinsic to the device, at a well-localized and known radial position within the plasma core in order to undertake impurity transport studies. Once deposited and exposed to the plasma, tracer particles are ablated by the plasma and the resultant clouds of semi-ionized (tracer plasmoids) particles will expand toroidally along the magnetic field lines until the tracer plasmoid and background plasma pressures equalize. The ablation cloud expansion velocity had been estimated by analysing the optical emission of ionized carbon (C^{2+}) in [16] to be approximately 8800 m s^{-1} parallel to the magnetic field, and ca. 1100 m s^{-1} perpendicular to it. It can be assumed that the actual high-z tracers are subject to similar processes, even if the velocities will differ due to the difference in mass compared to carbon.

Despite the investigation of diffusion and convection properties of W7-X plasmas and detailed transport analysis is outside the scope of this paper and will be left open to a future publication, some general aspects should be discussed here on behalf of experimental findings. Examples of soft x-ray emissivity signals, measured along selected sight-lines of the XMCTS diagnostics (cf figure 11) are shown in figure 12. The signals are characterized by oscillations, lasting for more than ten milliseconds and having frequencies in the order of about 1 kHz. While the signal of sight-line # 116 shows the highest oscillation amplitude, # 119 has the most intense signal and similar to # 125 also the steepest leading edge. Furthermore, a closer look to the lowermost diagram reveals a small peak, located at around 8010.5 ms with a width of about 70 μs, before the signals exhibit a steep rise in intensity (most prominent for the sight-lines # 117, # 119 and # 125).

A 2D tomographic reconstruction of all available XMCTS signals, superimposed on the local closed flux surfaces, is presented in figure 13. These plots reveal that the initial post-deposition x-ray emissions (upper left image, labelled 0.040) are localized in an area that is poloidally, but not radially, displaced from the initial intersection space of the magnetic field lines predicted for XMCTS and shown in figure 3. Starting with the sub-figure labelled 0.310, another narrowly limited area of most intense soft x-ray radiation begins to develop. Only with the last figure shown at the bottom right (label 0.590), the originally existing radiation asymmetries appear to have largely equilibrated along the flux surfaces. The time scale on which this process happens can be estimated from the damping of the oscillations in figure 12 and amounts to several 10 ms.

Similar radiation asymmetries were observed in plasma emissions, measured using bolometers, immediately after a cryogenic pellet injection into the stellarator TJ-II [40]. According to a friction- and inertia-based model developed in [40], a sudden breakdown of the advection/compression balance caused by the injection of the pellet led to emission asymmetries where an emission blob was seen to rotate about the magnetic axis during several milliseconds after the injection.

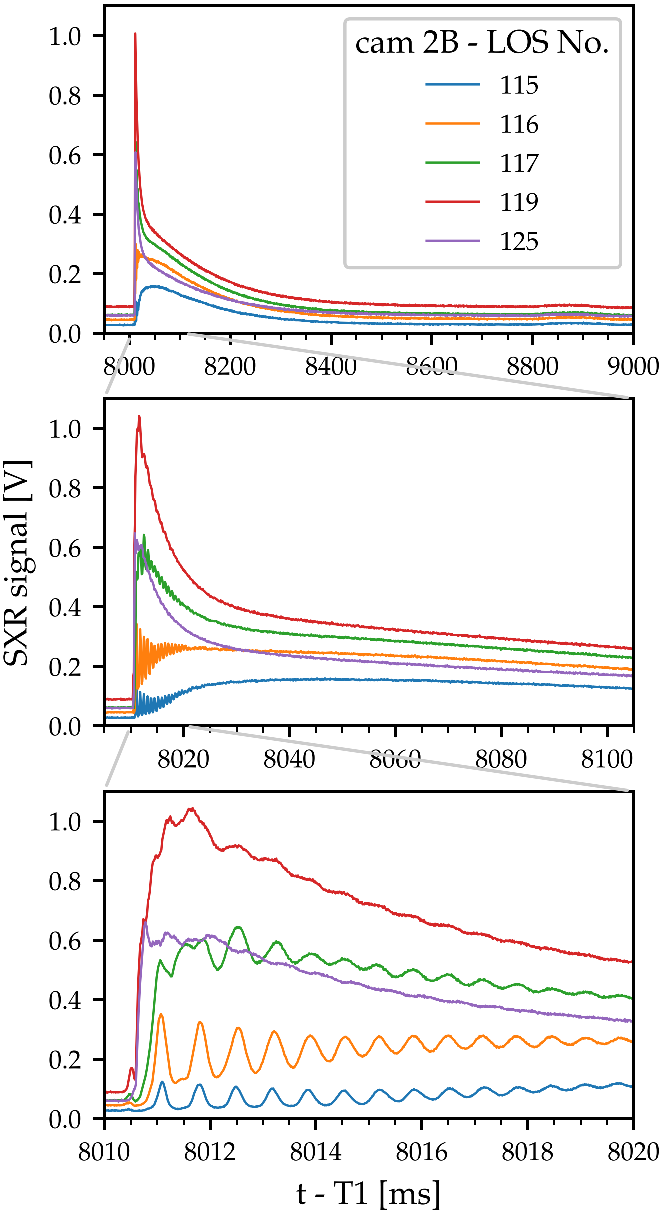

Figure 12. Temporal evolution of soft x-ray emissions along selected lines-of-sight (as indicated in figure 11).

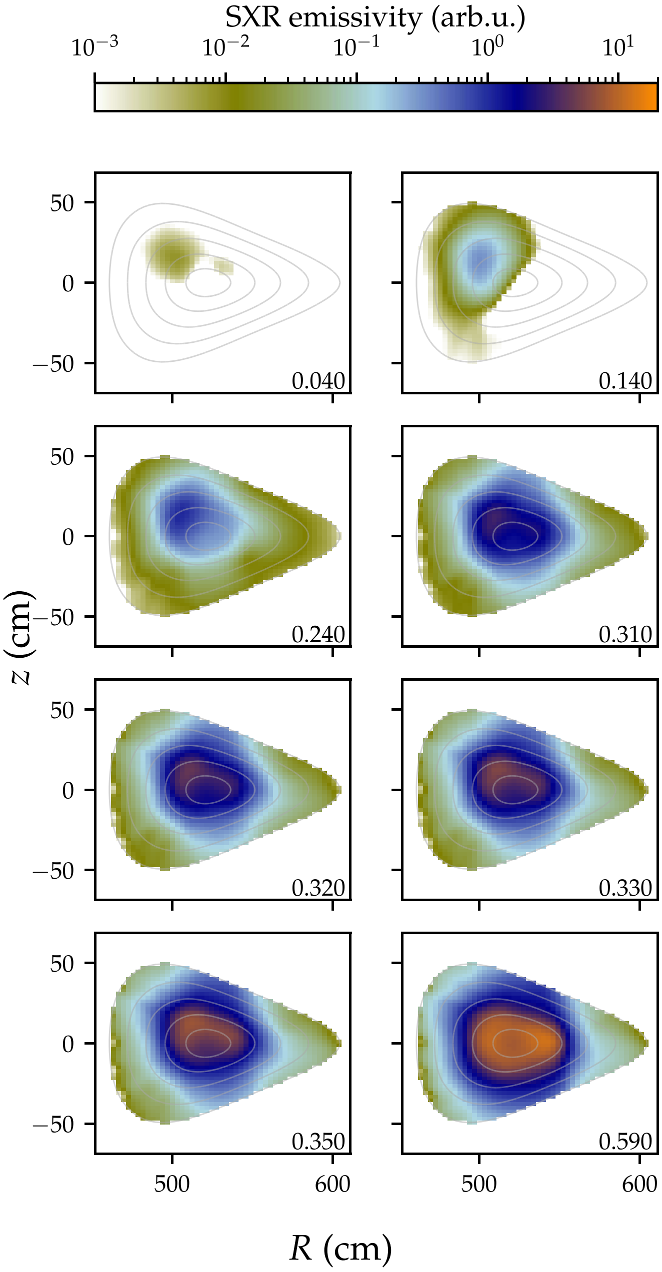

Figure 13. Temporal evolution of soft x-ray emissions, as detected by XMCTS, after the TESPEL injection into W7-X experiment #20 180 906.38 with positive magnetic field configuration (EJM001+252). Intensities, presented here correspond to the differences between the emissivity at the respective time instant and the averaged intensity distribution at the time of TESPEL arrival. Labels in the lower right corners of the sub-figures refer to the time in milliseconds after the arrival of the TESPEL in the confined plasma region. In comparison to the intersection points of the field lines, in the vicinity of which the ablated atoms/ions are initially released (see figure 3), the first, increased x-ray emissivities are observed here (see the upper left subfigure) with a slight poloidal offset in clockwise direction.

In the same work, the observed oscillation in the phase of the radiation asymmetry was reproduced by impurity fluid dynamic simulations and explained in terms of the advection of a decaying $m = 1$ asymmetry by the $\vec{E} \times \vec{B}$ flow. The oscillation characteristics seen in figure 12 is very similar to the one discussed for cryogenic pellets, so the physical effects causing them are assumed to be the same and $\vec{E} \times \vec{B}$ drift may then explain the observed poloidal shift in the initial post-deposition x-ray emissions.

Comparing the temporal evolution of the soft x-ray emissivity patterns in figure 13 with the signal evolution along specific sight-lines (figure 12) and also with the TESPEL ablation signals (figure 4) reveals further interesting details. The ablation of the injected TESPEL took about 300 μs for the shell and another 70 μs for the tracer. The signal maximum in figure 4(a) appears at about 250 μs to 300 μs after the ablation start. In figure 13 it takes about 300 μs (from label 0.040 to 0.310) until the strongest x-ray emissivities (faint orange area) become visible at R = 500–520 cm, z = 0–20 cm. This spatial range is covered by the selected sight-lines in figure 12. A comparison of the ablation signal characteristics with the

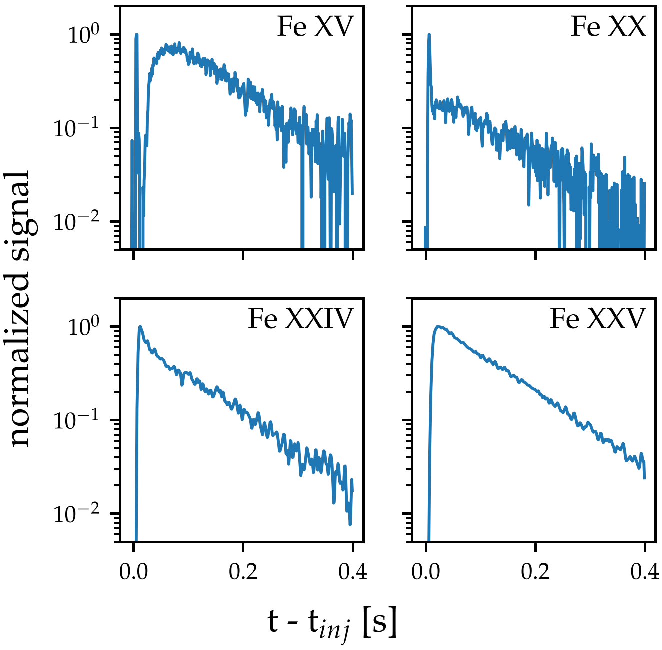

Figure 14. The temporal evolution of spectral line emissions from Fe XV, Fe XX, Fe XXIV and Fe XXV. Signals are normalized with respect to the maximum signal value. Here t_{inj} is the time when the Fe tracer is exposed to the hot plasma. The wavelengths of these lines are highlighted by an * in table 3.

temporal evolution of the XMCTS sight line signals suggests now, that the first three sub-figures in figure 13 (labelled 0.040 to 0.240) illustrate the x-ray emissivity changes during the TESPEL shell ablation (release of H and C), the one labelled 0.310 covers the transition phase between shell and tracer ablation, when high-Z materials (tracer load in this experiment: Fe + Si_3N_4) come into play and all further sub-figures depict the poloidal transport of tracer particles and finally their equilibration along the fluxsurfaces. Furthermore, based on the comparison of the above figures, it can be assumed that the first little peak in the line-of-sight signals mentioned at the beginning correlates with the ablation of the polystyrene shell and the steep rise in the signals afterwards represents the release of the tracer load and subsequent ionisation and transport.

Finally, figure 14 shows the temporal evolution of selected Fe spectral lines emitted by different ionization stages that were followed by the HEXOS and HR-XIS diagnostic. The signals are normalized to the maximum line emission intensities for each ionization state in the respective diagram. With Fe XV and Fe XX, there is an initial, short-lived intensity peak, followed by an immediate, rapid drop in intensity, which is then followed by a phase of constant decay. The initial transient peak is due to rapid multiple ionizations of the iron atoms, from the atomic state through to the He-like of H-like states, by plasma electrons in a volume where Te is of the order 1–2 keV. Then, as Fe ions are transported outwards across plasma regions of lower Te, recombination occurs and spectral lines emitted by lower ionization states of Fe reappear and decay. The analysis of latter phase, established about 100 ms after injection, where the signals of the different ionisation states begin to show similar decay behaviour, allows impurity confinement times to be determined. At present, such an analysis is being undertaken with the STRAHL transport code and findings will be reported in a future publication. This code solves the radial continuity for each impurity ionization stage in a 1D geometry and, in doing so, calculates radial transport.

4. Conclusion

A TESPEL injector system has been installed and commissioned on the Wendelstein 7-X stellarator. A successful transfer probability of 89% for intact TESPELs is reported. It is found experimentally that the successful injection of a 'shell-type' TESPEL with an outer diameter of 0.7 mm, loaded with Si_3N_4/Fe tracer particles (Fe-amount: 1.66×10^{17} atoms) into plasma with a line-integrated density of $4 \times 10^{19}\,\mathrm{m}^{-2}$ (line-averaged density $= 3 \times 10^{19}\,\mathrm{m}^{-2}$) results in a 5% perturbation in density, this being in very good agreement with predictions of 4%–5%. It is seen also that a sharp reduction in electron temperature concurs with the increase in plasma density due to the ablation processes and the deposition of cold electrons. However, unlike the density perturbation, which requires several hundreds of milliseconds to return to its pre-injection value, core electron temperatures return to within a few percent of pre-injection values after several 10's of milliseconds. Thus, it is considered that injections of TESPELs with adequate size and tracer content will result in acceptable changes in the plasma core transport conditions that are to be investigated.

When it comes to the theoretical description of the impurity transport, many models assume compliance with the trace limit ($\alpha = n_z Z^2/n_i \ll 1$) [41]. This boundary condition is significantly more limiting with regard to the experimental conditions for typical TESPEL injections than the plasma perturbation limit. The impurity strength $\alpha = n_z Z^2/n_i$, due solely to the contribution of the polystyrene of the outer TESPEL shell, is a factor of ≈ 5.3 above the curves for plasma perturbation shown in figure 2, so that even with the shell type S700 an $\alpha < 0.1$ can only be achieved at plasma densities above $5 \times 10^{19}\,\mathrm{m}^{-3}$. To estimate the actual tracer impurity strength, the calculation of the impurity concentration of the respective ionization stages is necessary, taking into account the given ionization conditions and temperature profiles, respectively. Therefore, for the theoretical description of the impurity transport and for modelling of the transport parameters, strict attention must be paid to the impurity level under the given experimental conditions and to the suitability of the model. This is particularly important considering the fact that when a TESPEL is injected, at least two different tracer materials (carbon from the polystyrene shell and the actual tracer material) are introduced into the plasma. The complexity may increase due to the possibility of filling TESPELs with up to three different chemical elements or even complex compounds at the same time. Furthermore, due to the expected large local density perturbation immediately after the ablation of TESPEL tracer particles, a strongly localised, but transient, violation of the tracer limit must be taken into consideration when undertaking analysis. The specific influence of various TESPEL properties (shell geometry, specific tracer load, tracer material) on turbulent transport behaviour is outside the scope of this Paper. It will be determined in future investigations. For further aspects on impurity transport modelling, especially under conditions where the tracer limit is not met, we refer to the works of Angioni [41] and Reinke [42].

Through careful consideration and analysis of TESPEL flight-path trajectories, filterscope signals, as well as kinetic plasma profiles and their confidence levels, uncertainties in the determination and prediction of the radial location of tracer exposure to the plasma have been estimated, i.e. $\Delta\rho = \pm 0.05$, for the investigated injection experiment. Moreover, it is shown that the use of different polystyrene capsule types and sizes for W7-X provides some flexibility for the pre-selection of the tracer penetration depth. From the injections made to date, the related radii of tracer release have ranged from $\rho \approx 0.32$ to 0.6 for 'S700' capsule types and from $\rho \approx 0.25$ to 0.42 for 'B900' types. These locations are well within the core plasmas and thus such injections avoid complications that arise in transport analysis due to the initial inward transport of the source as occurs when gas-puff or laser blow-off injections are performed.

In conclusion, it is considered that the TESPEL method will prove to be a powerful tool for undertaking impurity transport studies in future experimental campaigns on the Wendelstein 7-X stellarator device. In particular the problems arising from the broad band filters causing poor spectral separation between the different detection channels of our filterscope had been addressed in the meantime. With a new set of narrowband filters having bandwidths of about 1 nm FWHM, we expect a precise separation between shell and tracer ablation signals. Furthermore, also the fastcam system had been upgraded, providing now a second line-of-sight, such that a 2D reconstruction of the TESPEL injection trajectory will become possible with Wendelstein 7-X's experimental campaign OP2.2.

Data availability statement

The data cannot be made publicly available upon publication because no suitable repository exists for hosting data in this field of study. The data that support the findings of this study are available upon reasonable request from the authors.

Acknowledgments

This work has been carried out within the framework of the EUROfusion Consortium, funded by the European Union via the Euratom Research and Training Programme (Grant Agreement No. 101052200—EUROfusion). Views and opinions expressed are however those of the author(s) only and do not necessarily reflect those of the European Union or the European Commission. Neither the European Union nor the European Commission can be held responsible for them. One of the authors, KJM, acknowledges that this work is partially financed by Grant PID2020-116599RB-I00 funded by MCIN/AEI/10.13039/501100011033. Another author, NT, acknowledges financial support from the JSPS KAKENHI 17KK0121, the NIFS/NINS Program for Enhancing Research Collaboration (UFEX105), the NIFS/NINS Young Researchers Supporting Program (UFEX106), the NIFS/NINS under Strategic International Research Exchange Promotion Program (UFEX402), and the NINS program of Promoting Research by Networking among Institutions (Grant No. 01411702).

ORCID iDs

R Bussiahn https://orcid.org/0000-0002-6408-0922
N Tamura https://orcid.org/0000-0003-1682-1519
K J McCarthy https://orcid.org/0000-0002-5881-1442
B Buttenschön https://orcid.org/0000-0002-9830-9641
C Brandt https://orcid.org/0000-0002-5455-4629
A Dinklage https://orcid.org/0000-0002-5815-8463
A Langenberg https://orcid.org/0000-0002-2107-5488

References

[1] Burhenn R *et al* 2009 *Nucl. Fusion* **49** 065005
[2] McCormick K *et al* 2002 *Phys. Rev. Lett.* **89** 015001
[3] Ido T *et al* 2010 *Plasma Phys. Control. Fusion* **52** 124025
[4] Wolf R *et al* 2017 *Nucl. Fusion* **57** 102020
[5] Hathiramani D *et al* 2018 *Fusion Eng. Des.* **136** 304–8
[6] Nakamura Y *et al* 2003 *Nucl. Fusion* **43** 219
[7] Mattioli M, Giannella R, Myrnas R, Demichelis C, Denne-Hinnov B, Wit T D D and Magyar G 1995 *Nucl. Fusion* **35** 1115
[8] Kubkowska M *et al* 2017 *Fusion Eng. Des.* **136** 58–62
[9] Sudo S 1993 *J. Plasma Fusion Res.* **69** 1349
[10] Sudo S, Tamura N, Muto S, Funaba H, Suzuki C, Murakami A, Murakami I and Yoshimura Y and the LHD Experiment Group 2013 *Plasma Phys. Control. Fusion* **55** 095014
[11] Sudo S and Tamura N 2012 *Rev. Sci. Instrum.* **83** 023503
[12] Tamura N *et al* 2016 *Rev. Sci. Instrum.* **87** 11D619
[13] Bussiahn R, Tamura N, McCarthy K J, Burhenn R, Hayashi H, Laube R and Klinger T and LHD Experiment Group and W7-X Team 2018 *Rev. Sci. Instrum.* **89** 10K112
[14] Laube R, Bussiahn R, Tamura N and McCarthy K J 2020 *Fusion Eng. Des.* **150** 111259
[15] Kubkowska M *et al* 2020 *J. Instrum.* **15** C01019
[16] Kocsis G *et al* 2021 *Nucl. Fusion* **61** 016006
[17] Klinger T *et al* 2019 *Nucl. Fusion* **59** 112004
[18] Endler M *et al* 2021 *Fusion Eng. Des.* **167** 112381
[19] Bräuer T and the Metrology Team 2013 *Fusion Eng. Des.* **88** 721–4
[20] Schacht J, Laqua H, Müller I, Puttnies H and Skodzik J 2019 *IEEE Trans. Nucl. Sci.* **66** 969–73
[21] MDSplus (available at: http://mdsplus.org)
[22] Pégourié B 2007 *Plasma Phys. Control. Fusion* **49** R87
[23] Matsuyama A, Koechl F, Pegourie B, Sakamoto R, Motojima G and Yamada H 2012 *Plasma Fusion Res.* **7** 1303006
[24] McCarthy K J *et al* 2017 *Europhys. Lett.* **120** 25001
[25] Geiger J, Beidler C D, Feng Y, Maaßberg H, Marushchenko N B and Turkin Y 2015 *Plasma Phys. Control. Fusion* **57** 014004
[26] Hirshman S, van RIJ W I and Merkel P 1986 *Comput. Phys. Commun.* **43** 143–55
[27] Goto M, Sakamoto R and Morita S 2007 *Plasma Phys. Control. Fusion* **49** 1163

[28] Khlopenkov K V and Sudo S 1998 *Rev. Sci. Instrum.* **69** 3194–8
[29] Sergeev V Y, Bakhareva O A, Kuteev B V and Tendler M 2006 *Plasma Phys. Rep.* **32** 363–77
[30] Krychowiak M *et al* 2016 *Rev. Sci. Instrum.* **87** 11D304
[31] Biel W, Bertschinger G, Burhenn E, König R and Jourdain E 2004 *Rev. Sci. Instrum.* **75** 3268-3275
[32] Langenberg A *et al* 2018 *Rev. Sci. Instrum.* **89** 10G101
[33] Kramida A, Ralchenko Y and Reader J (NIST ASD Team) 2022 Nist atomic spectra database (version 5.10) (https://physics.nist.gov/asd)
[34] Brandt C *et al* 2020 *Plasma Phys. Control. Fusion* **62** 035010
[35] Anton M, Weisen H, Dutch M J, von der Linden W, Buhlmann F, Chavan R, Marletaz B, Marmillod P and Paris P 1996 *Plasma Phys. Control. Fusion* **38** 1849
[36] Jabłoński S, Czarnecka A, Kubkowska M, Ryc L, Weller A, Biedermann C and König R (the W7-X Team) 2015 *J. Instrum.* **10** 10021
[37] Bozhenkov S *et al* 2020 *Nucl. Fusion* **60** 066011
[38] Ford O *et al* 2024 *Nucl. Fusion* **64** 086067
[39] Carralero D *et al* 2021 *Nucl. Fusion* **61** 096015
[40] Alonso J A *et al* 2016 *Plasma Phys. Control. Fusion* **58** 074009
[41] Angioni C 2021 *Plasma Phys. Control. Fusion* **63** 073001
[42] Reinke M 2011 Experimental tests of parallel impurity transport theory in tokamak plasmas *PhD Thesis* Plasma Science and Fusion Center, Massachusetts Institute of Technology p PSFC/RR-11-14